2024 IEEE International Conference on Robotics and Automation (ICRA 2024)
May 13-17, 2024. Yokohama, Japan

NeRF-VINS: A Real-time Neural Radiance Field Map-based Visual-Inertial Navigation System

Saimouli Katragadda[1], Woosik Lee[1], Yuxiang Peng[1], Patrick Geneva[1], Chuchu Chen[1], Chao Guo[2], Mingyang Li[2], and Guoquan Huang[1]

***Abstract*— Achieving efficient and consistent localization with a prior map remains challenging in robotics. Conventional keyframe-based approaches often suffer from sub-optimal viewpoints due to limited field of view (FOV) and/or constrained motion, thus degrading the localization performance. To address this issue, we design a real-time tightly-coupled Neural Radiance Fields (NeRF)-aided visual-inertial navigation system (VINS). In particular, by effectively leveraging the NeRF's potential to synthesize novel views, the proposed NeRF-VINS overcomes the limitations of traditional keyframe-based maps (with limited views) and optimally fuses IMU, monocular images, and synthetically rendered images within an efficient filter-based framework. This tightly-coupled fusion enables efficient 3D motion tracking with bounded errors. We extensively validate the proposed NeRF-VINS against the state-of-the-art methods that use prior map information, and demonstrate its ability to perform real-time localization, at 15 Hz, on a resource-constrained Jetson AGX Orin embedded platform.**

I. Introduction

The ability to achieve high-accuracy localization is pivotal for edge devices which have become prevalent through computation miniaturization enabling AR/VR [1], [2] and consumer drones [3], [4]. The ubiquitous use of cameras and inertial measurement units (IMU) due to their low cost, low power, and small size makes the Visual-Inertial Navigation System (VINS) a critical component for the aforementioned applications [5]. If no global information (e.g., GPS, loop-closures, or a prior map), VINS can only provide ego-motion tracking with ever-growing error. Over the past two decades, a particular focus has been placed on leveraging *a priori* map as additional costly sensors are not required [6]–[12].

A crucial component of successful map-based localization is an accurate place retrieval algorithm such as DBoW [13], placeless [14], or NetVLAD [15], which allows for recovery of correspondence information to construct constraints to historical information. However, these methods may be vulnerable to viewpoint variations, poor viewpoint coverage limiting recall, scene ambiguities, and sensitivities to environmental changes after mapping [16].

To address these challenges, in this work, we propose to avoid the need for place recognition via the rendering of novel synthetic views adjacent to the current state estimate, enabling high-quality and informative loop-closure constraints that are not susceptible to these failure modes. Specifically, we introduce a new paradigm for map-based localization which leverages the recent Neural Radiance Fields (NeRF) [17] advancements in deep learning to compress the collection of images, e.g. a prior keyframe image map, into a trained network, and then leverage during localization the high-fidelity image rendering of synthesize novel camera viewpoints. While the NeRF's ability to accurately reconstruct complex environments has encouraged researchers to build dense NeRF maps [18], [19], we focus on achieving real-time localization on edge devices with limited computational resources and thus look to leverage the comparably cheaper novel viewpoint rendering via hashing [20]. To this end, we effectively leverage NeRF as an *a priori* map and maintain real-time drift-free VINS localization. The main contribution of this work includes:

- We, for the first time, develop a real-time NeRF-VINS algorithm that fuses *a priori* NeRF-based map in a tightly-coupled manner to enable drift-free localization.
- We conduct extensive numerical studies to understand the impact of different NeRF map construction methods, descriptor algorithms on rendered NeRF views, and environmental changes, thus better informing our design.
- The proposed NeRF-VINS is among the first to demonstrate centimeter-level drift-free pose estimates on an edge platform (Jetson AGX Orin rendering at over 10 Hz) and outperform existing state-of-the-art methods.

II. Related Work

In this section, we provide an overview of methods related to visual and visual-inertial and NeRF-based localization.

A. Prior Map-based Classical Localization

Single-View Visual Localization: The classical structure-based method is the Perspective-n-Point (PnP) solver within a RANSAC loop for robustness [21], [22]. The 2D-3D correspondences between the query image and a map points are typically found through the matching of local feature descriptors [23]–[27]. To mitigate the complexity increase as the map size grows, image retrieval methods that narrow down the search space typically retrieve top similar matches (place recognition) and query keypoints in the region defined by these images for correspondences (local matching) [8], [28]. The quality of this approach heavily relies on the effectiveness of the image retrieval methods. DBoW [13] has gained great popularity thanks to its efficiency, but recent deep learned-based HF-Net [8], which leverages NetVLAD [15] and SuperPoint [29] for global retrieval and local matching respectively, has demonstrated state-of-the-art

This work was partially supported by the University of Delaware (UD) College of Engineering, Delaware NASA/EPSCoR Seed Grant, NSF (IIS-1924897, SCH-2014264), and Google ARCore.

[1]The authors are with the Robot Perception and Navigation Group (RPNG), University of Delaware, Newark, DE 19716. Email: {saimouli, woosik, yxpeng, pgeneva, ccchu, ghuang}@udel.edu.

[2]The authors are with Google, Mountain View, CA 94043. Email: {chaoguo, mingyangli} @google.com.

performance in localization tasks. Although there are end-to-end deep learning methods available, their poor accuracy and complexity still make structure-based methods appealing [30]–[32]. Additionally, all discussed methods can suffer from global descriptor ambiguities, particularly in scenarios with sparse images or significant changes in viewpoint, and poor recall due to limited view coverage of the scene which we aim to address through the proposed NeRF-VINS rendering paradigm.

Visual-Inertial Localization: As compared to single-view visual localization, visual-inertial localization aims to continuously provide estimates against a prior map and can leverage historical information to reduce the search space and thus complexity. There is a rich literature, for which we refer the interested reader to the references in [9] for a summary. One which is of particular relevance to this work is the open-sourced ROVIOLI [11] extension of ROVIO [33], [34] which performs 2D-3D matches against an optimized global map commonly constructed using `maplab` [11], [12].

SLAM Systems: In contrast to previous approaches that construct maps offline for accurate localization, SLAM builds maps online and utilizes them via loop closures. A typical SLAM architecture includes a real-time thread for camera pose tracking using sparse keypoints [35], [36] or dense/semi-dense representations [37], [38], along with a non-real-time thread that optimizes and constructs the map. These methods use classical image retrieval techniques to query images for loop closure, which can be affected by limited viewpoint coverage and ambiguities.

B. Neural Radiance Fields

The work [17] introduced the NeRF methodology and revolutionized scene representation, novel view generation, and high-fidelity rendering. Later works such as BARF [39] and NeRF [40] have shown that knowing the exact poses is not required, while iMAP [41] and NICE-SLAM [42] showed that the joint optimization of poses in respect the NeRF can further improve performance. There additionally have been works that have focused on map representation [18], and the integration within SLAM [19], [43].

As compared to the online generation of NeRF maps, we instead look to leverage a previously built NeRF to provide high-quality loop-closure information and bound estimator drift. Only a few works have focused on leveraging NeRF to provide prior environmental information for the betterment of visual tracking. iNeRF [44] proposed to localize camera poses by optimizing the photometric error between the real and NeRF-generated images within a small static environment context but remained sensitive to the initial pose guess and large computational cost. More recently, Loc-NeRF [45] was proposed to employ a particle filter to remove the need for an initial guess. While this method does not require any initial guess, it necessitates image rendering for each particle, which could easily become computationally prohibitive if using a large number of particles. Another work similar spirit is by Adamkiewicz et al. [46] which leveraged a pre-trained NeRF map to localize and additionally optimize future trajectories. As compared to these works which are constrained by rendering speed and their alignment computational complexity, the proposed NeRF-VINS combines the novel viewpoint rendering strength with the efficient, and accurate MSCKF-based VINS.

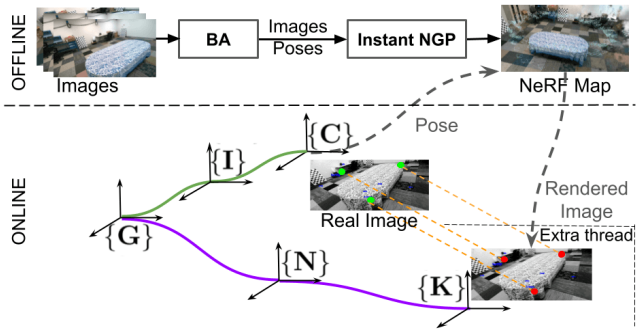

Fig. 1: Overview of the proposed NeRF-VINS, where $\{G\}$ is the global VIO frame, $\{N\}$ is the map frame, $\{K\}$ denotes the NeRF rendered image. $\{I\}$ and $\{C\}$ are IMU and camera frame, respectively. *Click on the image for a video demo.*

III. NeRF-VINS Estimator Design

Visual-inertial localization uses two main approaches: graph optimization [36], [47] and filter-based methods [10], [12], [48]. Graph optimization generally offers good accuracy, but is computationally demanding. In contrast, filter-based approaches like the MSCKF [48] efficiently integrate camera and IMU measurements, suitable for real-time applications. The MSCKF balances feature efficiency, avoiding complexity growth, making it ideal for resource-constrained real-time localization. The proposed NeRF-VINS estimator extends the MSCKF [48], [49] to fuse the prior NeRF map in a tightly-coupled manner (see Fig. 1). As such, for presentation brevity, in the following, we will primarily focus on visual measurement update.

In particular, at time t_k, the system state $\mathbf{x}_k$ consists of the current inertial navigation states $\mathbf{x}_{I_k}$, historical IMU poses $\mathbf{x}_{T_k}$, and a subset of 3D environmental point features, $\mathbf{x}_f$:

$$\mathbf{x}_k = \begin{bmatrix}\mathbf{x}_{I_k}^\top & \mathbf{x}_{T_k}^\top & \mathbf{x}_f^\top\end{bmatrix}^\top, \mathbf{x}_f = \begin{bmatrix}{}^G\mathbf{p}_{f_1}^\top & \cdots & {}^G\mathbf{p}_{f_i}^\top\end{bmatrix}^\top \quad (1)$$

$$\mathbf{x}_{I_k} = \begin{bmatrix}{}^{I_k}_{G}\bar{q}^\top & {}^G\mathbf{p}_{I_k}^\top & {}^G\mathbf{v}_{I_k}^\top & \mathbf{b}_g^\top & \mathbf{b}_a^\top\end{bmatrix}^\top \quad (2)$$

$$\mathbf{x}_{T_k} = \begin{bmatrix}{}^{I_k}_{G}\bar{q}^\top & {}^G\mathbf{p}_{I_k}^\top & \cdots & {}^{I_{k-c}}_{G}\bar{q}^\top & {}^G\mathbf{p}_{I_{k-c}}^\top\end{bmatrix}^\top \quad (3)$$

where ${}^I_G\bar{q}$ is the unit quaternion (${}^I_G\mathbf{R}$ in rotation matrix form) that represents the rotation from the global $\{G\}$ to IMU frame $\{I\}$. ${}^G\mathbf{p}_I$, ${}^G\mathbf{v}_I$, and ${}^G\mathbf{p}_{f_i}$ are the IMU position, velocity, and i'th point feature position in $\{G\}$; $\mathbf{b}_g$ and $\mathbf{b}_a$ are the gyroscope and accelerometer biases. Note that other state variables can be included, e.g., spatial-temporal calibration, but have been omitted for clarity.

The state is propagated over time based on the IMU measurements. A canonical three-axis IMU provides linear acceleration, ${}^I\mathbf{a}_m$, and angular velocity measurements, ${}^I\boldsymbol{\omega}_m$. The IMU nonlinear kinematics is generically given by [50]:

$$\mathbf{x}_{I_{k+1}} = \mathbf{f}\left(\mathbf{x}_{I_k}, {}^I\mathbf{a}_k, {}^I\boldsymbol{\omega}_k, \mathbf{n}_{I_k}\right) \quad (4)$$

where $\mathbf{n}_{I_k} = [\mathbf{n}_g^\top \ \mathbf{n}_a^\top \ \mathbf{n}_{wg}^\top \ \mathbf{n}_{wa}^\top]^\top$; $\mathbf{n}_g$ and $\mathbf{n}_a$ are Gaussian white noises, and $\mathbf{n}_{wg}$ and $\mathbf{n}_{wa}$ are the random walk bias noises of gyroscope and accelerometer, respectively. With this model (4), we can perform EKF propagation of the state estimate and covariance [48].

A. Measurement Update with Real Images

As in [49], bearing measurements of detected features seen at time t_k are modeled as follows:

$$\mathbf{z}_{C_k} = \mathbf{h}_c(\mathbf{x}_{T_k}, {}^G\mathbf{p}_f) + \mathbf{n}_{C_k} := \mathbf{\Lambda}({}^{C_k}\mathbf{p}_f) + \mathbf{n}_{C_k} \quad (5)$$

$${}^{C_k}\mathbf{p}_f = {}^C_I\mathbf{R}\ {}^{I_k}_G\mathbf{R}({}^G\mathbf{p}_f - {}^G\mathbf{p}_{I_k}) + {}^C\mathbf{p}_I \quad (6)$$

where $\mathbf{\Lambda}\left([x\ y\ z]^\top\right) = \begin{bmatrix} x/z & y/z \end{bmatrix}^\top$ and $\mathbf{n}_{C_k}$ is the white Gaussian noise. Linearizing Eq. (5) yields the following measurement residual:

$$\mathbf{r}_{C_k} = \mathbf{z}_{C_k} - \mathbf{h}_c(\hat{\mathbf{x}}_{T_k}, {}^G\hat{\mathbf{p}}_f) \quad (7)$$

$$\simeq \mathbf{H}_{T_k}\tilde{\mathbf{x}}_{T_k} + \mathbf{H}_{f_k}{}^G\tilde{\mathbf{p}}_f + \mathbf{n}_{C_k} \quad (8)$$

where $\mathbf{H}_T$ and $\mathbf{H}_f$ are the Jacobian matrix of the measurement with respect to each state. We keep the long-tracked features in the state till lost in order to leverage their future observations, while the short-tracked features are updated via the efficient MSCKF nullspace projection [48].

B. Measurement Update with NeRF Images

When a camera image reading is received, a NeRF render is triggered at a pose with a small horizontal positional offset (e.g., 10 cm, as in our experiments, in analogy to a stereo baseline) to the current camera pose. This synthetic image should have a *significant* overlapping field of view (FOV) with the current real image, which facilitates high-quality feature matching. The small positional offset also enables robust triangulation and accurate feature matching between the real and synthetic images even when the camera is static.

Once the rendering is completed, descriptor-based feature matching is performed to the current image, where a 2D-to-2D prior keyframe measurement model is leveraged [51]. For example, consider that from the rendered image we get a bearing measurement, $\mathbf{z}_{N_k}$, which is related by [see (5)]:

$$\mathbf{z}_{N_k} = \mathbf{h}_n\left({}^G\mathbf{p}_f\right) + \mathbf{n}_{N_k} := \mathbf{\Lambda}({}^K\mathbf{p}_f) + \mathbf{n}_{N_k} \quad (9)$$

$${}^K\mathbf{p}_f = {}^K\mathbf{p}_N + s{}^K_N\mathbf{R}({}^N\mathbf{p}_G + {}^N_G\mathbf{R}{}^G\mathbf{p}_f) \quad (10)$$

where s is the scale factor of the map and $\mathbf{n}_{N_k}$ is the zero mean Gaussian noise. Note that we model the bearing as only a function of the feature ${}^G\mathbf{p}_f$, and consider the map transform $\{s, {}^N_G\mathbf{R}, {}^N\mathbf{p}_G\}$ to be known (see Sec. IV-C) and the rendered camera pose $\{{}^K_N\mathbf{R}, {}^K\mathbf{p}_N\}$ to have some known orientation and position error $\{{}^N_G\tilde{\boldsymbol{\theta}},\ {}^N\tilde{\mathbf{p}}_G\}$. Thus, we have the following linearized model:

$$\mathbf{r}_{N_k} = \mathbf{z}_{N_k} - \mathbf{h}_n({}^G\hat{\mathbf{p}}_f) = s\mathbf{H}_{\mathbf{\Lambda}}{}^K_N\mathbf{R}{}^N_G\mathbf{R}{}^G\tilde{\mathbf{p}}_f + \mathbf{n}'_{N_k} \quad (11)$$

$$\mathbf{n}'_{N_k} = s\mathbf{H}_{\mathbf{\Lambda}}{}^K_N\mathbf{R}(\lfloor {}^N_G\mathbf{R}{}^G\mathbf{p}_f \times \rfloor {}^N_G\tilde{\boldsymbol{\theta}} + {}^N\tilde{\mathbf{p}}_G) + \mathbf{n}_{N_k} \quad (12)$$

where $\mathbf{H}_{\mathbf{\Lambda}}$ is the measurement jacobian in respect to the 3D point feature and $\lfloor\cdot\times\rfloor$ is the skew-symmetric matrix. The linearized model can be used to update the features in the state or can be stacked with the real image measurements (8) to perform (SLAM or MSCKF) EKF update.

IV. System Integration

Armed with the NeRF-VINS estimation theory presented in the previous section, we now describe how to integrate the NeRF model and feature matching between synthetic and real images to form a tightly-coupled system.

In particular, our system leverages the open-source Instant-NGP [20] for rendering and prior map training. The Open-VINS [49] frontend is modified to incorporate SuperPoint

Fig. 2: Example rendered images for testing matching methods. *Left*: Rendered image with resolution 424×240. *Right*: Rendered image with 141×80 resolution and up-scaled to 424×240 with FSRCNN [52].

TABLE I: Average descriptor extraction time, number of matches, and ATE reported on the UD AR Table 1-8 dataset [60] for different matching methods utilizing the configuration depicted on the right side of Fig. 2.

	AKAZE	BRISK	ORB	KAZE	SP	SP Opt.
Time (ms)	31	88	13	140	15	7
No. of Matches	55	85	20	117	31	30
ATE (deg/m)	2 FAIL	5 FAIL	6 FAIL	2.40 / 0.29	1.16 / 0.15	1.18 / 0.16

descriptors using Tensor-RT pipeline [53]. We used OpenCV [54] and CUDA to convert GPU-rendered images to a 32bit-float RGB image on the CPU. Additional care has been taken to convert the NeRF-rendered image coordinate system to a right-hand coordinate system by inverting the y and z axes of InstantNGP. The code is written in C++ and CUDA and runs on Jetson AGX Orin unless specified.

A. Feature Descriptor Selection

A crucial component is the ability to match features between the current frame and the rendered NeRF viewpoint. Thus significant effort has been spent to investigate the performance of various feature matching methods such as AKAZE [55], KAZE [56], BRISK [57], ORB [58], and the selected SuperPoint (SP) [29]. For this test, we choose a challenging scenario by rendering at (141×80) and upscaling to 424×240 using FSRCNN [52], see Fig. 2. Shown in Tab. I, the average descriptor extraction time, number of matches between the rendered and current camera image, and Absolute Trajectory Error (ATE) [59] of VINS for each method have been compared. It is clear that the handcrafted matching methods (AKAZE, BRISK, ORB, and KAZE) often fail and show large errors which is expected due to the limited fidelity in the up-sampled resolution NeRF image. On the other hand, SuperPoint (SP) and its optimized variant (SP Opt.) are shown to be robust to these conditions and report the highest accuracy and shortest descriptor extraction time. We thus select the optimized SuperPoint for its robustness and efficiency for synthetic NeRF to real image matching.

B. Image Rendering and Feature Matching

Rendering NeRF images remains a computationally expensive operation even with state-of-the-art techniques [20]. On embedded devices like the Jetson AGX Orin, it takes approximately 660ms (2Hz) to render an image with dimensions 424×240. To improve render speed and minimize loop-closure latency, we use a two-step process. Initially, we generate NeRF renders at half resolution (212×140). Then, we employ the lightweight FSRCNN [52] for up-sampling to the original size of 424×240. This approach strikes a balance between computational speed and image quality (see Fig.

(a) DBoW (b) NetVLAD (c) Ours

Fig. 3: Qualitative study of failure cases of classical place recognition method. Green and Red lines indicate inliers and outliers, respectively. Input image (left of each column) and retrieved, rendered for the NeRF case (resolution 212×140 and upsampled to 424×240), image is shown (right of each column). Images are shown in color for visualization purposes.

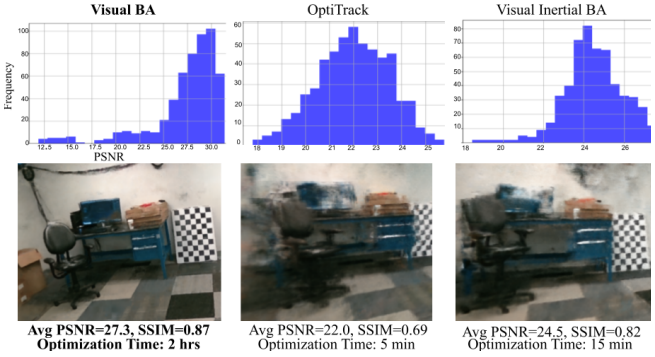

Fig. 4: Qualitative comparison of NeRF Map trained with different methods using 543 keyframe images. The top row shows the PSNR histograms and the bottom row shows exemplary images rendered from each method.

2 and Tab. I for the extreme case of 141×80 resolution). We further reduce the resolution levels and the hashing size of the model in InstantNGP [20] and minimize multiple CPU copies by directly transferring rendered images to our localization pipeline for descriptor extraction.

The rendering is run on a separate thread to prevent blocking of the real-time VINS. The SuperPoint feature matching network has been modified to use a lightweight ResNet18 [61] and optimized to support a 16-bit floating point using TensorRT [53]. This secondary thread, which performs rendering and matching, runs at 15Hz on the Jetson. Additional timing details are reported in [62].

C. Offline NeRF Map Generation

Another foundational component is the ability to build and train a prior NeRF map which can be leveraged online (see Fig. 1 top half). The first challenge is to recover accurate camera poses which can then be used in conjunction with images to train the NeRF model. Three different methods were investigated: (i) Visual Bundle Adjustment (BA) via COLMAP [26], [27], (ii) Visual-Inertial BA via `maplab` [12], and (iii) fusion of OptiTrack poses with IMU via *vicon2gt* [63]. We leveraged the keyframing selection in `maplab` to select a subset of 543 of poses which both COLMAP and `maplab` optimized.

Analyzing the results of the Table 5 dataset in Fig. 4, we observe clear variation in Peak Signal-to-Noise Ratio (PSNR) and Structural Similarity Index (SSIM) [17]. COLMAP's up-to-scale Visual BA yields superior values, albeit at the expense of significant computation to optimize the camera poses. Conversely, the Visual-Inertial BA in `maplab` did take less time to optimize, but suffers in PSNR whose blurriness can be seen in the exemplary images. A similar trend is observed in the *vicon2gt* OptiTrack+IMU results, indicating that while the fusion of inertial information accelerates optimization time and provides scale information, it does not improve visual reconstruction quality, likely due to calibration and sensor synchronization errors in this dataset. We additionally conjecture that IMU-aided methods likely do not fully minimize visual reprojection errors to the same degree as COLMAP, potentially leading to suboptimal poses for desired geometric reprojection errors crucial for high-quality NeRF creation. We thus opted to use the up-to-scale COLMAP poses for training the NeRF. These poses were aligned to the groundtruth poses based on similarity transformation (sim3) to remove the scale ambiguity. For each dataset we assume that the proposed NeRF-VINS has been initialized in the NeRF prior map and directly leverage a pre-computed map transform.

V. Experimental Validation

We validate the proposed NeRF-VINS and baseline methods on the recently released AR Table Dataset [60]. This dataset is ideal for NeRF reconstruction due to its object-centric trajectories which observe a table placed centrally. This dataset additionally enables us to evaluate the robustness of algorithms to changing environments (see Fig. 5), due to the addition of a whiteboard for the three datasets (Table 5-7) and the moving of the table to the side of the room in Table 8. Unless specifically noted, all prior map methods leverage Table 1 for datasets 1-4 and Table 5 for 5-7.

Fig. 5: Exemplary environment configurations in [60].

In particular, for comprehensive validation, we evaluated the following state-of-the-art methods:

*1) **Single-Shot Visual Localization**:* The open-source Hierarchical Localization (HLoc) system [8] that used NetVLAD for image retrieval, and SuperPoint [29] descriptor establishes a baseline for expected state-of-the-art performance. In this system, local matching is performed using a nearest-neighbor search with a ratio test and geometric verification, which aligns with our pipeline. Notably, the use of Lightglue [64] matching remains computationally expensive (16 ms for a pair, thus 800 ms for top 50 on A3000 GPU) and did not yield substantially better results in the evaluated dataset. The same images and poses that are used to train the NeRF are leveraged in its map. We evaluated the performance with the top 5 and 50 nearest neighbor matches: HLoc (top5) and HLoc (top50), respectively. Due to its single-shot nature, we found that for many image localization accuracy was poor, and thus in most results presented we select an inlier set of good quality success to provide a reasonable comparison. Note that this contrasts the below map-based methods and proposed NeRF-VINS which provide *continuous* estimates.

*2) **Map-based Visual-Inertial Localization**:* For map-based VINS, the filter-based ROVIO with additional re-localization module [34] (ROVIOLI) from `maplab` [12] provides one of the closest direct comparisons to the proposed method. We report the accuracy of both the odometry, ROVIOLI, and the map-aided, ROVIOLI+Map, which leverages the `maplab` optimized prior map with the same keyframes used to train the NeRF. VINS-Fusion (VF) [65], is additionally compared against as it has support to re-localization against a previous-built relative pose graph using DBoW2 [13]. Thus we run VF on the prior map dataset to generate a pose graph that is then leveraged for sequential datasets (e.g. the whole dataset Table 1 is processed, as compared to the proposed which uses only a small subset of keyframes). Both the odometry, VF, the secondary pose graph without relocalization, VF+Loop, and then the secondary thread which is able to relocalize against the prior map pose graph, VF+Loop+Map, are evaluated.

A. Localization Accuracy

Tab. II shows the ATE of all methods including the proposed method on our desktop (termed Nerf-VINS (D)) equipped with an A4500 NVIDIA graphics card and on Jetson AGX Orin (termed Nerf-VINS (J)), we also provide odometry methods as a reference to show that we are able to improve the system we build on (i.e OpenVINS). It is clear that our proposed method achieved one of the best accuracy over all algorithms while HLoc showed competing results (note we excluded large failures of HLoc from statistics). An interesting observation is that VF reported higher accuracy than VF+Loop which was due to multiple false loop closures induced by incorrect DBoW matching. This poor performance is shown by other methods which leverage DBoW, showing the need for novel view synthesis.

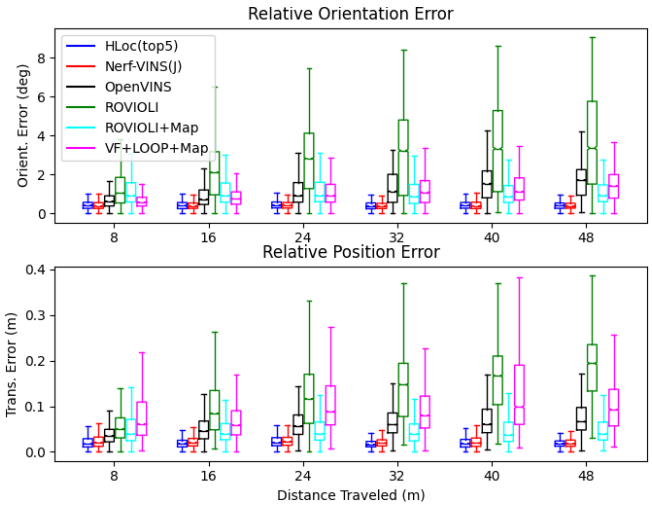

Fig. 6: Boxplot of the RPE [59] statistics run with the same setting as Tab. II. The box spans the first and third quartiles, while the whiskers are the upper and lower limits.

The Relative Pose Error (RPE) [59] over all datasets (see Fig. 6) highlights the significant advantage of incorporating NeRF map features, which effectively mitigates drift and maintains bounded error. We attribute this performance gain to the proposed method's ability to render informative novel scenes resulting in good viewpoints and a good number of quality measurements (Fig. 3). Though HLoc was able to provide good accuracy, there were many failures that were excluded from the statistics, and moreover, the classification of inliers and outliers for real-time estimation is challenging.

B. Computational Complexity

We additionally investigated the average timing of each function of our system and compared it with HLoc. Note that we disabled the multi-threading of the proposed NeRF-VINS and compare on the same system for a fair comparison. The results reported in Tab. III show the total time of the proposed system takes 30 ms which is almost half of the total timing of HLoc with top 5 match results. Though the performance of HLoc can be improved by retrieving more images, this will introduce a significant computation burden for local matching and PnP, making it difficult to run in real-time (HLoc (top 50) pipelines take 331.9 ms per frame as shown in Tab. III). This clearly shows that our pipeline is lightweight and is capable of high-rate rendering of the NeRF images enabling real-time localization fully leveraging the NeRF map information.

C. Robustness to Environment Changes

To assess our system in generating favorable viewpoints enabling robust localization even when the environment is changed after mapping, we examined a more challenging scenario: employing Table 1 as the map and running on Table 5-8 each with distinct environments (refer to Fig. 5). Our system shows robust localization performance which is also competitive with HLoc (note that HLoc encounters numerous

TABLE II: The ATE of each algorithm on the AR Table dataset (degree/cm). The top two best results are highlighted with a bold green color.

	Algorithms	Table 1	Table 2	Table 3	Table 4	Table 5	Table 6	Table 7	Average
Map-based	Nerf-VINS (D)	0.51 / 1.8	0.27 / 1.0	0.50 / 1.0	0.35 / 1.5	0.43 / 1.4	0.59 / 1.9	0.46 / 1.6	**0.44** / **1.5**
	Nerf-VINS (J)	0.47 / 2.0	0.29 / 0.8	0.50 / 0.9	0.31 / 1.6	0.43 / 1.3	0.54 / 1.9	0.51 / 1.7	**0.44** / **1.5**
	VF+Loop+Map	0.93 / 4.1	1.27 / 7.1	0.88 / 6.1	1.39 / 5.2	0.72 / 3.2	0.93 / 3.7	1.68 / 5.3	1.11 / 5.0
	ROVIOLI+Map	0.54 / 2.1	1.30 / 3.6	0.67 / 2.2	1.15 / 4.3	0.86 / 3.7	2.33 / 17.9	2.42 / 13.6	1.32 / 6.8
	HLoc (top5)*	0.41 / 1.0	0.40 / 1.6	0.38 / 1.4	0.31 / 1.3	0.41 / 1.2	0.60 / 1.6	0.51 / 2.0	0.48 / 1.4
	HLoc (top50)*	0.41 / 1.0	0.33 / 1.4	0.35 / 1.2	0.30 / 1.2	0.40 / 1.2	0.57 / 1.6	0.51 / 2.0	**0.45** / **1.3**
VINS	OpenVINS	1.17 / 5.4	0.55 / 2.2	1.02 / 3.4	1.21 / 5.9	0.50 / 3.3	1.04 / 3.7	1.31 / 7.2	0.97 / 4.5
	ROVIOLI	2.05 / 7.1	1.11 / 4.1	2.63 / 7.9	1.48 / 11.1	2.50 / 12.1	1.10 / 4.3	3.12 / 15.9	2.00 / 8.9
	VF+Loop	1.25 / 6.7	1.18 / 9.2	0.95 / 6.5	1.10 / 5.7	0.88 / 2.8	0.98 / 11.2	1.57 / 10.1	1.13 / 7.5
	VF	1.62 / 5.8	1.32 / 3.0	1.47 / 7.6	1.75 / 5.6	1.12 / 3.4	0.98 / 5.3	1.67 / 9.3	1.42 / 5.7

* Large failures (errors larger than 5 degrees or 10 cm) of HLoc (top5) and HLoc (top50) are excluded from statistics:
HLoc (top5) failure rates: Table 2 37%, Table 3 5.5%, Table 4 0.4%, Table 5 0.5%, Table 6 1%, Table 7 0.5%
HLoc (top50) failure rates: Table 2 39%, Table 3 2.4%, Table 4 0.4%

TABLE III: Average timing for proposed NeRF-VINS and HLoc pipeline in milliseconds. Recorded on a laptop with A3000 GPU and 11th Gen Intel(R) Core(TM) i7-11800H @ 2.30GHz CPU.

Step	Nerf-VINS (D)	HLoc (top 5)	HLoc (top 50)
Tracking	8.5	-	-
Rendering / NetVLAD	11.6	12.9	12.9
Superpoint Extraction	5.4	7.6	7.6
Local Matching	1.7	15.2	153.7
Update / PnP	2.5	21.3	157.7
Total	29.8	57.0	331.9

TABLE IV: AR table ATE (degree/cm) and Table 1 is used as a map for the following sequence. Blanks indicate failures. The top two best results are indicated with bold green color.

Algorithm	Table 5	Table 6	Table 7	Table 8	Average
Nerf-VINS (J)	0.49 / 3.0	0.61 / 4.1	0.54 / 3.3	0.38 / 3.0	**0.50** / **3.4**
HLoc (top5)*	0.61 / 3.5	0.64 / 3.6	0.61 / 3.1	0.50 / 3.7	**0.59** / 3.5
HLoc (top50)*	0.65 / 3.4	0.67 / 3.6	0.62 / 3.0	0.47 / 3.1	0.60 / **3.3**
VF+Loop+Map	0.95 / 12.4	0.82 / 3.3	1.60 / 9.3	2.44 / 9.9	1.45 / 8.7
ROVIOLI+Map	2.48 / 11.3	1.89 / 12.9	2.59 / 14.8	- / -	2.32 / 13.0

* HLoc error larger than 5 degrees or 10 cm are removed to be presentable
HLoc(top5) failure rates: Table 5 38.9%, Table 6 36.8%, Table 7 37.1%, Table 8 30.5%
HLoc(top50) failure rates: Table 5 23.9%, Table 6 29.4%, Table 7 21.8%, Table 8 10.7%

failures, which are omitted from consideration see Tab. IV). In contrast, our system consistently delivers advantageous viewpoints, facilitating large inlier measurements (Fig. 3).

As can be seen from Fig. 7, around 80% percent of images for our pipeline are localized within a 2.5 cm accuracy threshold, while HLoc is only around 70% when matching with the top 50 images. Our system can localize almost all the images within a 7.5 cm position error, while HLoc using the top 5 images and top 50 can only localize 80.9% and 89.3% images within a 20 cm error bound, respectively.

D. Discussion and Limitations

We observe that rendering images at adjacent poses generates more matches between the rendered image and the camera image compared to queried database images like those in DBoW. This suggests that the rendered image, being pose-based, is less influenced by scene ambiguities, particularly noticeable during environmental changes in Fig. 3. The results presented in Fig. 4 raise intriguing considerations

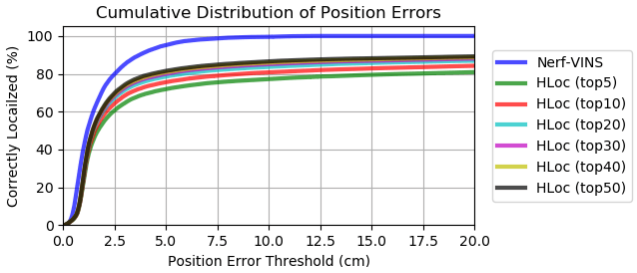

Fig. 7: The percentage of images successfully localized under a certain position error threshold using Table 1 as a map to evaluate Table 1-8.

and challenges regarding the necessity to expedite training time while preserving rendering quality in joint optimization. Additionally, studying the sensitivity of IMU noise and its effects on rendering quality and joint optimization costs warrants further in-depth investigation. While we have demonstrated that the proposed method exhibits superior localization performance, similar to other NeRF methods, our map is also object-centric. To train the map effectively, requires surrounding images for effective training. One potential solution is to leverage F2-NerF [66] and Block-Nerf [67], designed for unbounded camera trajectories and large-scale map training. Recent works such as Kerbl et al. [68] offer greater rendering speed and open a new avenue for exploration. We leave these as future work.

VI. Conclusions and Future Work

In this paper, we have developed a real-time tightly-coupled NeRF-VINS algorithm. Built on top of the MSCKF, the proposed NeRF-VINS extends to efficiently and accurately fuses the NeRF synthetic images to overcome the limited viewpoint challenges commonly encountered by the keyframe map-based localization methods. In particular, as NeRF can generate novel views from any viewpoint, we exploit this advantage to synthesize better views to provide higher inlier matches that allow for full utilization of the map information, resulting in performance gain. In the future, we will investigate NeRF map-based initialization i.e., initializing the transform between the IMU and map frames.

REFERENCES

[1] Google, "ARCore," https://developers.google.com/ar.

[2] Apple, "ARKit," https://developer.apple.com/augmented-reality/.

[3] S. Katragadda, B. A. Mondal, and A. Deane, "Stereoscopic mixed reality in unmanned aerial vehicle search and rescue," in *AIAA Scitech 2019 Forum*, 2019, p. 0154.

[4] C. Chen, Y. Yang, P. Geneva, W. Lee, and G. Huang, "Visual-inertial-aided online mav system identification," in *IEEE/RSJ International Conference on Intelligent Robots and Systems (IROS)*, 2022.

[5] G. Huang, "Visual-inertial navigation: A concise review," in *Proc. International Conference on Robotics and Automation*, Montreal, Canada, May 2019.

[6] S. Lynen, T. Sattler, M. Bosse, J. A. Hesch, M. Pollefeys, and R. Siegwart, "Get out of my lab: Large-scale, real-time visual-inertial localization." in *Robotics: Science and Systems*, vol. 1, 2015, p. 1.

[7] A. Kasyanov, F. Engelmann, J. Stückler, and B. Leibe, "Keyframe-based visual-inertial online slam with relocalization," in *2017 IEEE/RSJ international conference on intelligent robots and systems (IROS)*. IEEE, 2017, pp. 6662–6669.

[8] P.-E. Sarlin, C. Cadena, R. Siegwart, and M. Dymczyk, "From coarse to fine: Robust hierarchical localization at large scale," in *CVPR*, 2019.

[9] P. Geneva and G. Huang, "Map-based visual-inertial localization: A numerical study," in *Proc. International Conference on Robotics and Automation*, Philadelphia, USA, May 2022.

[10] A. I. Mourikis, N. Trawny, S. I. Roumeliotis, A. E. Johnson, A. Ansar, and L. Matthies, "Vision-aided inertial navigation for spacecraft entry, descent, and landing," *IEEE Transactions on Robotics*, 2009.

[11] T. Schneider, M. T. Dymczyk, M. Fehr, K. Egger, S. Lynen, I. Gilitschenski, and R. Siegwart, "maplab: An Open Framework for Research in Visual-inertial Mapping and Localization," *IEEE Robotics and Automation Letters*, vol. 3, no. 3, pp. 1418–1425, 2018.

[12] A. Cramariuc, L. Bernreiter, F. Tschopp, M. Fehr, V. Reijgwart, J. Nieto, R. Siegwart, and C. Cadena, "maplab 2.0 – A Modular and Multi-Modal Mapping Framework," *IEEE Robotics and Automation Letters*, vol. 8, no. 2, pp. 520–527, 2023.

[13] D. Gálvez-López and J. D. Tardós, "Bags of binary words for fast place recognition in image sequences," *IEEE Transactions on Robotics*, 2012.

[14] S. Lynen, M. Bosse, P. Furgale, and R. Siegwart, "Placeless place-recognition," in *2014 2nd International Conference on 3D Vision*, vol. 1. IEEE, 2014, pp. 303–310.

[15] R. Arandjelovic, P. Gronat, A. Torii, T. Pajdla, and J. Sivic, "NetVLAD: Cnn architecture for weakly supervised place recognition," in *Proceedings of the IEEE conference on computer vision and pattern recognition*, 2016, pp. 5297–5307.

[16] K. Li, Y. Ma, X. Wang, L. Ji, N. Geng, *et al.*, "Evaluation of global descriptor methods for appearance-based visual place recognition," *Journal of Robotics*, vol. 2023, 2023.

[17] B. Mildenhall, P. P. Srinivasan, M. Tancik, J. T. Barron, R. Ramamoorthi, and R. Ng, "Nerf: Representing scenes as neural radiance fields for view synthesis." ECCV, 2020.

[18] C. Jiang, H. Zhang, P. Liu, Z. Yu, H. Cheng, B. Zhou, and S. Shen, "H2-mapping: Real-time dense mapping using hierarchical hybrid representation," 2023.

[19] C.-M. Chung, Y.-C. Tseng, Y.-C. Hsu, X.-Q. Shi, Y.-H. Hua, J.-F. Yeh, W.-C. Chen, Y.-T. Chen, and W. H. Hsu, "Orbeez-slam: A real-time monocular visual slam with orb features and nerf-realized mapping," in *2023 IEEE International Conference on Robotics and Automation (ICRA)*. IEEE, 2023, pp. 9400–9406.

[20] T. Müller, A. Evans, C. Schied, and A. Keller, "Instant neural graphics primitives with a multiresolution hash encoding," *ACM Transactions on Graphics (ToG)*, vol. 41, no. 4, pp. 1–15, 2022.

[21] O. Chum, J. Matas, and J. Kittler, "Locally optimized ransac," in *Pattern Recognition: 25th DAGM Symposium, Magdeburg, Germany, September 10-12, 2003. Proceedings 25*. Springer, 2003.

[22] O. Chum and J. Matas, "Optimal randomized ransac," *IEEE Transactions on Pattern Analysis and Machine Intelligence*, 2008.

[23] T. Sattler, B. Leibe, and L. Kobbelt, "Fast image-based localization using direct 2d-to-3d matching," in *2011 International Conference on Computer Vision*, 2011.

[24] L. Liu, H. Li, and Y. Dai, "Efficient global 2d-3d matching for camera localization in a large-scale 3d map," in *2017 IEEE International Conference on Computer Vision (ICCV)*, 2017.

[25] T. Sattler, B. Leibe, and L. Kobbelt, "Efficient & effective prioritized matching for large-scale image-based localization," *IEEE Transactions on Pattern Analysis and Machine Intelligence*, 2017.

[26] J. L. Schonberger and J.-M. Frahm, "Structure-from-motion revisited," in *Proceedings of the IEEE conference on computer vision and pattern recognition*, 2016, pp. 4104–4113.

[27] J. L. Schönberger, E. Zheng, M. Pollefeys, and J.-M. Frahm, "Pixelwise view selection for unstructured multi-view stereo," in *European Conference on Computer Vision (ECCV)*, 2016.

[28] M. Humenberger, Y. Cabon, N. Guerin, J. Morat, V. Leroy, J. Revaud, P. Rerole, N. Pion, C. de Souza, and G. Csurka, "Robust image retrieval-based visual localization using kapture," *arXiv preprint arXiv:2007.13867*, 2020.

[29] D. DeTone, T. Malisiewicz, and A. Rabinovich, "Superpoint: Self-supervised interest point detection and description," in *Proceedings of the IEEE conference on computer vision and pattern recognition workshops*, 2018.

[30] A. Kendall, M. Grimes, and R. Cipolla, "Posenet: A convolutional network for real-time 6-dof camera relocalization," in *Proceedings of the IEEE international conference on computer vision*, 2015, pp. 2938–2946.

[31] A. Kendall and R. Cipolla, "Geometric loss functions for camera pose regression with deep learning," in *Proceedings of the IEEE conference on computer vision and pattern recognition*, 2017, pp. 5974–5983.

[32] L. Yang, Z. Bai, C. Tang, H. Li, Y. Furukawa, and P. Tan, "Sanet: Scene agnostic network for camera localization," in *Proceedings of the IEEE/CVF international conference on computer vision*, 2019, pp. 42–51.

[33] M. Bloesch, S. Omari, M. Hutter, and R. Siegwart, "Robust visual inertial odometry using a direct ekf-based approach," in *2015 IEEE/RSJ international conference on intelligent robots and systems (IROS)*. IEEE, 2015, pp. 298–304.

[34] M. Bloesch, M. Burri, S. Omari, M. Hutter, and R. Siegwart, "Iterated extended kalman filter based visual-inertial odometry using direct photometric feedback," *The International Journal of Robotics Research*, 2017.

[35] G. Klein and D. Murray, "Parallel tracking and mapping for small AR workspaces," in *Proc. Sixth IEEE and ACM International Symposiumon Mixed and Augmented Reality*, 2007.

[36] S. Leutenegger, S. Lynen, M. Bosse, R. Siegwart, and P. Furgale, "Keyframe-based visual–inertial odometry using nonlinear optimization," *The International Journal of Robotics Research*, 2015.

[37] J. Engel, T. Schöps, and D. Cremers, "Lsd-slam: Large-scale direct monocular slam," in *European conference on computer vision*. Springer, 2014, pp. 834–849.

[38] C. Forster, M. Pizzoli, and D. Scaramuzza, "SVO: Fast semi-direct monocular visual odometry," in *IEEE International Conference on Robotics and Automation (ICRA)*, 2014.

[39] C.-H. Lin, W.-C. Ma, A. Torralba, and S. Lucey, "Barf: Bundle-adjusting neural radiance fields," in *IEEE International Conference on Computer Vision (ICCV)*, 2021.

[40] Z. Wang, S. Wu, W. Xie, M. Chen, and V. Adrian Prisacariu, "Nerf−−: Neural radiance fields without known camera parameters," *arXiv preprint arXiv:2102.07064*, 2021.

[41] E. Sucar, S. Liu, J. Ortiz, and A. Davison, "iMAP: Implicit mapping and positioning in real-time," in *Proceedings of the International Conference on Computer Vision (ICCV)*, 2021.

[42] Z. Zhu, S. Peng, V. Larsson, W. Xu, H. Bao, Z. Cui, M. R. Oswald, and M. Pollefeys, "Nice-slam: Neural implicit scalable encoding for slam," in *Proceedings of the IEEE/CVF Conference on Computer Vision and Pattern Recognition (CVPR)*, 2022.

[43] A. Rosinol, J. J. Leonard, and L. Carlone, "NeRF-SLAM: Real-time dense monocular slam with neural radiance fields," *arXiv preprint arXiv:2210.13641*, 2022.

[44] L. Yen-Chen, P. Florence, J. T. Barron, A. Rodriguez, P. Isola, and T.-Y. Lin, "iNeRF: Inverting neural radiance fields for pose estimation," in *IEEE/RSJ International Conference on Intelligent Robots and Systems (IROS)*, 2021.

[45] D. Maggio, M. Abate, J. Shi, C. Mario, and L. Carlone, "Loc-nerf: Monte carlo localization using neural radiance fields," in *IEEE International Conference on Robotics and Automation*. IEEE, 2023.

[46] M. Adamkiewicz, T. Chen, A. Caccavale, R. Gardner, P. Culbertson, J. Bohg, and M. Schwager, "Vision-only robot navigation in a neural radiance world," *IEEE Robotics and Automation Letters*, 2022.

[47] T. Qin, P. Li, and S. Shen, "Vins-mono: A robust and versatile monocular visual-inertial state estimator," *IEEE Transactions on Robotics*, 2018.

[48] A. I. Mourikis and S. I. Roumeliotis, "A multi-state constraint kalman filter for vision-aided inertial navigation," in *Proceedings 2007 IEEE International Conference on Robotics and Automation*, 2007.

[49] P. Geneva, K. Eckenhoff, W. Lee, Y. Yang, and G. Huang, "OpenVINS: a research platform for visual-inertial estimation," in *Proc. of the IEEE International Conference on Robotics and Automation*, Paris, France, 2020. [Online]. Available: https://github.com/rpng/open_vins

[50] A. B. Chatfield, *Fundamentals of High Accuracy Inertial Navigation*. Reston, VA: American Institute of Aeronautics and Astronautics, Inc., 1997.

[51] P. Geneva, K. Eckenhoff, and G. Huang, "A linear-complexity EKF for visual-inertial navigation with loop closures," in *Proc. International Conference on Robotics and Automation*, Montreal, Canada, May 2019.

[52] C. Dong, C. C. Loy, and X. Tang, "Accelerating the super-resolution convolutional neural network," in *Computer Vision–ECCV 2016: 14th European Conference, Amsterdam, The Netherlands, October 11-14, 2016, Proceedings, Part II 14*. Springer, 2016.

[53] NVIDIA, "TensorRT," https://github.com/NVIDIA/TensorRT.

[54] G. Bradski, "The OpenCV Library," *Dr. Dobb's Journal of Software Tools*, 2000.

[55] P. F. Alcantarilla and T. Solutions, "Fast explicit diffusion for accelerated features in nonlinear scale spaces," *IEEE Trans. Patt. Anal. Mach. Intell*, vol. 34, no. 7, pp. 1281–1298, 2011.

[56] P. F. Alcantarilla, A. Bartoli, and A. J. Davison, "KAZE features," in *Computer Vision–ECCV 2012: 12th European Conference on Computer Vision, Florence, Italy, October 7-13, 2012, Proceedings, Part VI 12*. Springer, 2012, pp. 214–227.

[57] S. Leutenegger, M. Chli, and R. Y. Siegwart, "BRISK: Binary robust invariant scalable keypoints," in *2011 International conference on computer vision*. IEEE, 2011, pp. 2548–2555.

[58] E. Rublee, V. Rabaud, K. Konolige, and G. Bradski, "ORB: An efficient alternative to sift or surf," in *2011 International conference on computer vision*. Ieee, 2011, pp. 2564–2571.

[59] Z. Zhang and D. Scaramuzza, "A tutorial on quantitative trajectory evaluation for visual (-inertial) odometry," in *2018 IEEE/RSJ International Conference on Intelligent Robots and Systems (IROS)*. IEEE, 2018, pp. 7244–7251.

[60] C. Chen, P. Geneva, Y. Peng, W. Lee, and G. Huang, "Monocular visual-inertial odometry with planar regularities," in *Proc. of the IEEE International Conference on Robotics and Automation*, London, UK., 2023. [Online]. Available: https://github.com/rpng/ar_table_dataset

[61] K. He, X. Zhang, S. Ren, and J. Sun, "Deep residual learning for image recognition," in *Proceedings of the IEEE conference on computer vision and pattern recognition*, 2016.

[62] S. Katragadda, W. Lee, Y. Peng, P. Geneva, C. Chen, and G. Huang, "NeRF-VINS: A real-time neural radiance field map-based visual-inertial navigation system," University of Delaware, Tech. Rep. RPNG-2023-NERF, 2023, available: http://udel.edu/~ghuang/papers/tr_nerf.pdf.

[63] P. Geneva and G. Huang, "vicon2gt: Derivations and analysis," University of Delaware, Tech. Rep. RPNG-2020-VICON2GT, 2020, available: http://udel.edu/~ghuang/papers/tr_vicon2gt.pdf.

[64] P. Lindenberger, P.-E. Sarlin, and M. Pollefeys, "LightGlue: Local Feature Matching at Light Speed," in *ICCV*, 2023.

[65] T. Qin, S. Cao, J. Pan, and S. Shen, "A general optimization-based framework for global pose estimation with multiple sensors," *arXiv preprint arXiv:1901.03642*, 2019.

[66] P. Wang, Y. Liu, Z. Chen, L. Liu, Z. Liu, T. Komura, C. Theobalt, and W. Wang, "F2-NeRF: Fast neural radiance field training with free camera trajectories," in *Proceedings of the IEEE/CVF Conference on Computer Vision and Pattern Recognition*, 2023, pp. 4150–4159.

[67] M. Tancik, V. Casser, X. Yan, S. Pradhan, B. Mildenhall, P. P. Srinivasan, J. T. Barron, and H. Kretzschmar, "Block-NeRF: Scalable large scene neural view synthesis," in *Proceedings of the IEEE/CVF Conference on Computer Vision and Pattern Recognition*, 2022, pp. 8248–8258.

[68] B. Kerbl, G. Kopanas, T. Leimkühler, and G. Drettakis, "3d gaussian splatting for real-time radiance field rendering," *ACM Transactions on Graphics*, vol. 42, no. 4, 2023.